ADVANCED MATERIALS TECHNOLOGIES
www.advmattechnol.de

Film-Based Multi-Photon Lithography for Efficient Printing of Electromagnetic Surface Structures

Gordon Zyla, Savvas Papamakarios, Dimitrios C. Zografopoulos, Anna Christoforidou, George Kenanakis, Maria Farsari, and Odysseas Tsilipakos**

This study introduces an approach, termed film-based multi-photon lithography (MPL), for the efficient fabrication of electromagnetic surface structures. Unlike conventional MPL, which utilizes droplet-shaped photosensitive volumes for the fabrication of 3D structures, this method employs photosensitive thin films to minimize the influence of axial voxel dimensions. This modification enables rapid printing of 2D surface structures over large areas with dry objective lenses, achieving feature sizes as small as 250 nm. The versatility of film-based MPL is demonstrated through the fabrication of terahertz metasurfaces featuring metallized split-ring resonators on glass substrates, as well as mid-infrared metasurfaces comprising dielectric pillars on silicon-on-insulator substrates. These structures are successfully produced over areas spanning cm^2 and mm^2 using a hybrid organic–inorganic photoresist within a maximum processing time of 2 h. Particularly with hybrid organic-inorganic photoresists, additional post-processing via calcination shows significant potential for producing purely inorganic periodic structures with reduced feature sizes. Moreover, film-based MPL enables the fabrication of high-resolution 2.5D surface structures, which are challenging to achieve using conventional lithographic methods. Experimental results are analyzed through profilometry, scanning electron microscopy, Fourier transform infrared spectroscopy, and energy- dispersive X-ray spectroscopy, while simulations confirmed the electromagnetic responses of the metasurfaces.

1. Introduction

Surface structures at the micro- and nanoscale exhibit remarkable potential for enabling diverse functionalities across various fields. Nature itself offers a prominent example, as organisms have developed sophisticated systems that employ these structures to achieve advanced optical and mechanical properties crucial for survival.[1,2]

While nature has long inspired biomimetic research and applications,[3–5] modern engineering is increasingly harnessing surface structures as a whole, driving innovative applications in fields such as biomedicine,[6] optics,[7] and energy regulation.[8] Additionally, a particularly exciting development in optics and photonics is the emergence of metasurfaces–periodically arranged electromagnetic structures at the micro- and nanoscale.[9] These structures facilitate strong light–matter interactions, allowing precise manipulation of the properties of electromagnetic radiation,

G. Zyla, S. Papamakarios, G. Kenanakis, M. Farsari
Institute of Electronic Structure and Laser
Foundation for Research and Technology-Hellas
Heraklion GR-70013, Greece
E-mail: zyla@iesl.forth.gr
G. Zyla
Laser Research Center, Physics Faculty
Vilnius University
Vilnius LT-10223, Lithuania

The ORCID identification number(s) for the author(s) of this article can be found under https://doi.org/10.1002/admt.202402137

DOI: 10.1002/admt.202402137

S. Papamakarios
Department of Physics National and Kapodistrian University of Athens
Athens GR-15784, Greece
D. C. Zografopoulos
School of Electrical and Computer Engineering
Aristotle University of Thessaloniki
Thessaloniki GR-54124, Greece
D. C. Zografopoulos
Consiglio Nazionale delle Ricerche
Istituto per la Microelettronica e Microsistemi
Rome IT-00133, Italy
A. Christoforidou
Lund University
Faculty of Engineering
Lund SE-22100, Sweden
O. Tsilipakos
Theoretical and Physical Chemistry Institute
National Hellenic Research Foundation
Athens GR-11635, Greece
E-mail: otsilipakos@eie.gr

including amplitude, phase, and polarization, solely through their geometry, material composition, and size. Typically fabricated from materials such as dielectrics or metals, though not exclusively limited to these, metasurfaces provide unprecedented control over light-matter interactions, significantly expanding possibilities for wavefront engineering.[10–13] In this context, metasurfaces have enabled new possibilities for creating flat counterparts to traditional optical components,[14–16] as well as perfect absorbers with selective electromagnetic responses, wavelength conversion, and optical switching, among other advanced applications.[17–21]

The fabrication of metasurfaces typically begins with the patterning of a photoresist. Conventional lithographic techniques, such as electron beam lithography, focused ion beam lithography, photolithography, and nanoimprint lithography, are widely utilized in this context due to their ability to achieve exceptionally high-resolution structures.[15,22,23] Despite their precision, these methods often require clean-room environments, vacuum conditions, harsh chemicals, and the use of exposure masks. Thus, they are associated with complex, costly, and time-intensive processes, which also limit their flexibility in producing diverse metasurface designs. For a comprehensive overview of the advantages and limitations of these lithographic techniques in metasurface fabrication, see refs. [22, 24].

Additionally, direct laser writing (DLW) using continuous wave (CW) diode lasers at 375 nm/405 nm provides a maskless, high-throughput method for efficient metasurface fabrication, addressing many of the challenges associated with conventional lithography.[24,25] However, the precision of DLW is inherently limited by the linear nature of its fabrication process. These constraints are primarily due to the optical diffraction limit and laser radiation scattering, which restrict both the achievable feature resolution and the minimum spacing between structures. For instance, commercially available DLW systems can achieve minimum feature sizes and spacings of 0.3 μm and 0.5 μm, respectively, but only when operated in high-resolution mode.[26,27] Such settings, however, substantially reduce fabrication speed, often restricting processing rates to a few mm^2/min. At higher writing speeds, the achievable feature resolution and minimum feature spacing typically approach or exceed 1 μm.[26,27]

A promising alternative to the aforementioned techniques for metasurface fabrication is multi-photon lithography (MPL).[28] Recent advancements have positioned MPL as an emerging printing technique for advanced applications across multidisciplinary research fields.[29] The significance of MPL extends beyond its role as a maskless, true 3D printing method; it relies on nonlinear absorption induced by ultrafast laser radiation.[30] This process enables the creation of ellipsoidally-shaped building blocks, known as voxels, at arbitrary positions within photosensitive materials upon threshold excitation. Notably, due to its nonlinear nature, MPL allows the generation of voxels smaller than the focal volume, with their longer axis aligned along the focusing direction, while their dimensions can be altered by adjusting the laser intensity. Thus, MPL theoretically offers higher precision in feature resolution and spacing compared to standard DLW, with further improvements achievable through dynamic laser intensity modulation.[31,32]

Nevertheless, when traditionally performed within a droplet-shaped volume of photosensitive material, MPL encounters significant challenges in efficiently fabricating planar structures, such as metasurfaces. While MPL has demonstrated remarkable potential for creating electromagnetic structures with 3D complexities,[33–37] for 2D planar surface structures, its applications have largely been confined to the printing of small areas designed for specific light–matter interactions.[38–41] Extending the fabrication of planar surface structures to the larger areas required for their practical use as a whole rather than for niche applications remains challenging, as these structures must exhibit high uniformity in arrangement, geometry, and dimensions.

The primary limitations in this context arise from MPL's core methodology–serially assembling individual voxels along predefined exposure paths derived from computer-generated models. This process requires precise control of voxel dimensions, both lateral and axial, to match the desired structural features. Thus, in most cases, traditional MPL involves a layer-by-layer fabrication approach, with each layer necessitating numerous exposure events. Achieving nanoscale precision further demands oil-immersion objective lenses with high numerical apertures (NA) while ensuring uniformity over larger areas requires autofocus systems and high-precision axes. These factors collectively render the traditional MPL process for fabricating surface structures both complex and relatively slow. Although recent advancements have improved MPL throughput,[42] they often involve trade-offs, such as lower axial resolution or reduced flexibility.[43–45]

This work addresses the challenges of creating functional electromagnetic surface structures by performing MPL in photosensitive thin films, referred to here as "film-based MPL." Recent studies have demonstrated the potential of film-based MPL for fabricating high-resolution structures (down to sub-100 nm) rapidly across diverse materials,[46] including metal-oxide semiconductors[47] and biodegradable materials.[48]

Building on this potential, the present study further highlights the advantages of film-based MPL, particularly when using dry objective lenses–including those with NA typically considered less suitable for high-resolution tasks (NA < 0.5)–in combination with hybrid organic–inorganic photoresists similar to SZ2080™, a widely used standard for 3D structuring in MPL.

In this configuration, film-based MPL enables the periodic polymerization of defined volumes into specific shapes optimized for interaction with electromagnetic radiation. This makes it a viable maskless fabrication method for producing functional metasurfaces across broad spectral ranges, particularly from the terahertz (THz) to mid-infrared (mid-IR) regime. Leveraging MPL's inherent adaptability, film-based MPL facilitates the rapid structuring of large areas, covering mm^2 to cm^2 scales, on various substrates, including those with reflective optical surfaces in the visible wavelength range.

Notably, employing hybrid organic-inorganic photoresists in film-based MPL enables the selective metallization of metasurfaces through electroless plating–an essential capability for realizing THz metasurfaces. Furthermore, the combination of film-based MPL and hybrid photoresists allows for the fabrication of periodic surface structures with reduced feature sizes through calcination, providing greater flexibility in designing and manufacturing complex metasurfaces.

Finally, this work expands the scope of film-based MPL beyond previous studies using photosensitive films by demonstrating its ability to create elevated features, such as micro-rings and

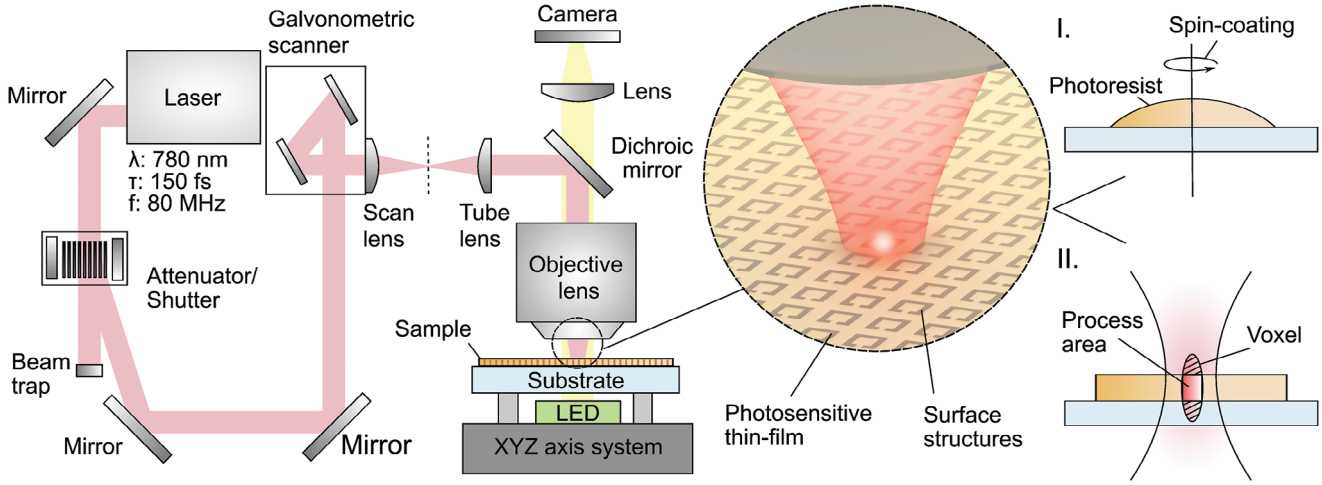

Figure 1. Schematic illustration of manufacturing surface structures via film-based MPL. The manufacturing principle for fabricating surface structures via film-based MPL involves processing a photosensitive thin film using fs laser radiation. The image on the left illustrates the MPL setup used, while a close-up view of the process area is shown in the center image. The photosensitive thin films were produced through spin-coating (I). When these films are considerably thin, the axial voxel dimension, as demonstrated in (II), does not affect the structuring and allows the lateral voxel size to be precisely adjusted to match the desired lateral feature size of the structure.

micro-disks residing on small pillars, without significantly compromising fabrication speed or precision. This capability extends its applicability beyond planar 2D structures, enabling the production of features with 2.5D complexities–an aspect particularly challenging to achieve with conventional lithographic techniques.

2. Methodologies of Film-Based MPL

2.1. Principle Method for Efficient Printing of Surface Structures Using MPL

When targeting the printing of surface structures with 2D or 2.5D complexity using MPL, employing photosensitive thin films instead of droplet-shaped photosensitive volumes significantly enhances flexibility and productivity. Specifically, these films ensure consistent printing conditions across the surface of a substrate, thereby broadening the practical applicability of MPL, particularly for non-transparent substrates like silicon-on-insulator (SOI), which are crucial in photonics but less commonly utilized in traditional MPL processes.

A key factor of film-based MPL for the efficient printing of surface structures is minimizing the influence of MPL's axial resolution, represented by the axial voxel dimension. As a result, film-based MPL is less sensitive to mechanical errors, such as substrate tilting, and enables rapid fabrication over large areas by significantly reducing the number of exposure events required to produce a structure. In particular, film-based MPL is highly effective for 2D surface structuring when the thickness of the photosensitive film is much smaller than the voxel length (see **Figure 1**, bottom right corner). Under these conditions, the number of exposure events per structure can be reduced to a single one, as the voxel width can be adjusted to match the feature size. Importantly, the minimum film thickness–typically ranging from sub-µm to several µm–aligns with the targeted minimum structural feature size, considering that the voxel length is generally at least three times greater than its width.[49]

Another key feature for improving printing efficiency with film-based MPL is that it allows the use of dry objective lenses with NAs below 1 while still achieving sub-µm lateral feature resolution, as detailed later. Compared to oil-immersion objectives, dry objective lenses provide a larger field of view (FOV), which is crucial for improving productivity by minimizing the need for stitching in MPL printing processes that utilize a 2D galvo scanner to address rapid fabrication requirements.

Notably, film-based MPL can be seamlessly realized with any optical setup capable of performing MPL. This is due to the simplicity of producing uniform photosensitive thin films via spin-coating, which can then be processed using a standard MPL setup, as illustrated in Figure 1. Specifically in this study, MPL was performed using a focused ultrashort-pulsed laser system operating at a central wavelength of 780 nm, with a pulse duration of 150 fs and a repetition rate of 80 MHz. Moreover, the experiments involved printing individual arrays that were stitched together to cover a large area. Individual arrays were fabricated either by directly scanning the laser beam to create the desired structural geometry or by selectively exposing specific areas for a defined duration. A 2D galvo scanner and a shutter facilitated the printing of individual arrays, while stitching was enabled by an XYZ-axis system. Additional details about experimental methods are provided in the Supporting Information.

In the majority of experiments, two types of hybrid zirconium (Zr)-based photoresists were employed in the experiments, with details of their synthesis (always in a total volume of 2 mL) provided in the SI. Both photoresists incorporated 2-(dimethylamino)ethyl methacrylate (DMAEMA) as an organic photopolymerizable monomer, mixed in specific ratios with zirconium n-propoxide (ZPO) to form an inorganic network. Notably, the use of DMAEMA offered distinct advantages in this context. For instance, previous studies showed that incorporating 10% DMAEMA relative to ZPO enhances MPL

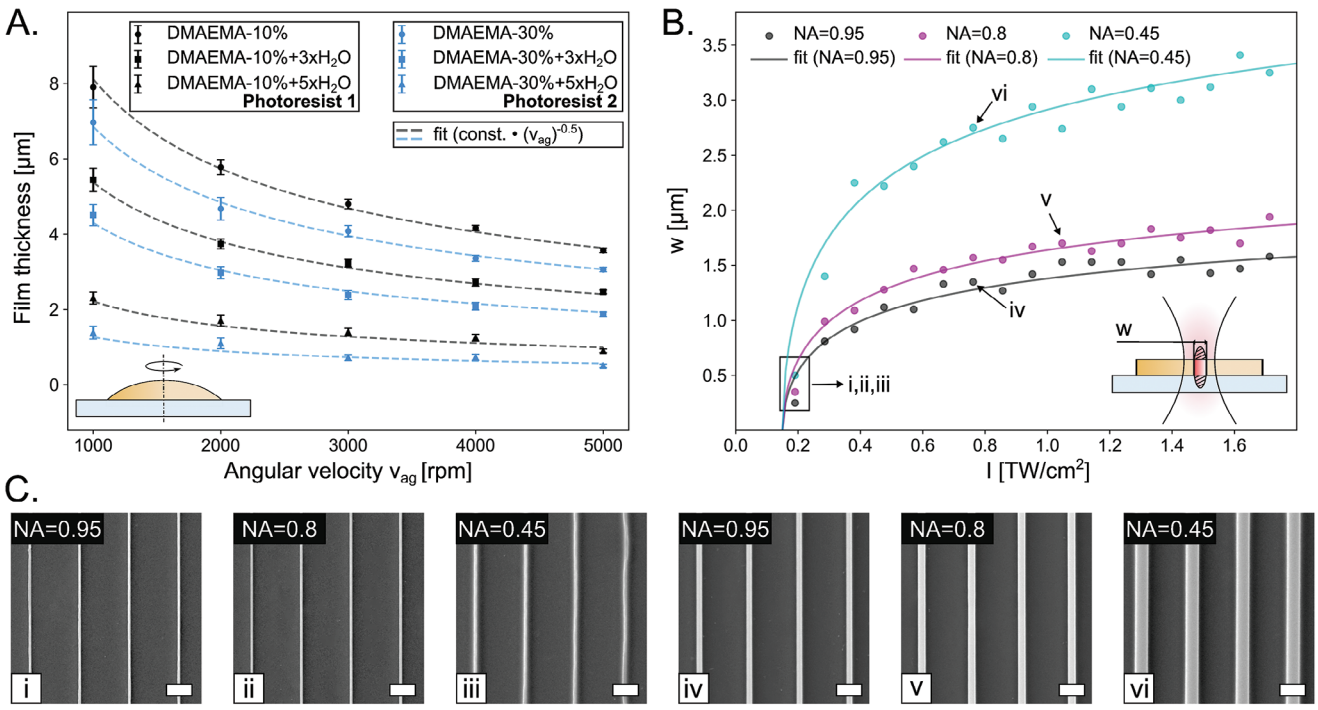

Figure 2. Spin-coated films and lateral feature resolution in film-based MPL. A) The resulting film thicknesses are plotted against the angular velocity v_{ag} used in the spin-coating process. The results are fitted according to *const.* · $(v_{ag})^{-0.5}$. B) Average widths of lines fabricated using different objective lenses are plotted as dots against the focal intensity used in film-based MPL. The writing speed was consistently set to 5 mm s^{-1} across all experiments. Theoretical approach to describe feature resolution in MPL was used as fit. C) SEM images of lines produced with different objective lenses and focal intensities are shown. Each set of lines is labeled with Roman numerals to correspond with the feature width labeled similarly in (B).

resolution due to its quenching properties.[50] In contrast, increasing the DMAEMA content to 30% promotes the formation of metal-binding moieties on MPL-printed structures via a post-processing approach, enabling selective electroless silver plating (SESP),[51] as also demonstrated in this study.

2.2. Film Preparation and Feature Resolution in Film-Based MPL

To implement film-based MPL and achieve films with thicknesses ranging from sub-µm to several µm for surface structuring, the relationship between spin-coating parameters–particularly angular velocity–and film thickness was systematically studied for photoresist 1 containing 10% DMAEMA and photoresist 2 containing 30% DMAEMA. Notably, throughout all experiments, including the printing of metasurfaces discussed later, spin-coating was consistently carried out using a fixed volume of 100 µl of these photoresists. Angular acceleration and spin-coating duration were set to 1000 rpm s^{-1} and 60 s, respectively. Additionally, all substrates were silanized prior to spin-coating, as detailed in the Supporting Information, to improve adhesion.

For the initial studies on achievable film thicknesses, standard coverslips (130–160 µm thick) were used and processed with angular velocity (v_{ag}) varied between 1000 and 5000 rpm. Tape masking was applied to small sections of the coverslips to enable profilometer measurements. Following spin-coating, the films were baked for 5 min at 40°C to evaporate residual solvents and subsequently cured under UV light (see Supporting Information for details). To confirm repeatability, three films were prepared for each parameter set under identical conditions.

The relationship between film thickness and angular velocity is depicted in **Figure 2A**, with error margins shown as vertical lines capped horizontally. The results align with the expected trend, demonstrating that film thickness decreases as angular velocity increases during spin-coating. This behavior follows the general relationship: film thickness ∝*const.* · $(v_{ag})^{-0.5}$, where the constant depends on the material's properties.

At higher angular velocities, the small error margins emphasize the process's consistency and reproducibility. In contrast, at lower angular velocities, the errors are more pronounced. While imperfections in drop-casting the material onto the substrate's center may have contributed to these variations, the primary cause is likely the material's characteristics. Since the material was not purely liquid, its properties significantly influenced the spin-coating dynamics, leading to greater variability in the results. This explanation is further supported by the observation that error margins are largest when the ratio between film thickness and angular velocity is higher. In such cases, the film thickness exhibited greater sensitivity to changes in angular velocity, amplifying the effect of any variations in material properties or process conditions.

When using the photoresists in their pure form, the minimum achievable film thicknesses were limited to approximately 3.0 and 3.5 µm, respectively (circular markers in Figure 2A). To achieve

thinner films, the photoresists were diluted with distilled water during synthesis in proportions based on the total monomer volume (see Supporting Information). As shown in Figure 2A, increasing the distilled water content in the photoresists enabled thinner films through spin-coating. The optimal conditions for producing thin films were achieved by adding five parts distilled water. Under these conditions, at an angular velocity of 5000 rpm, minimum film thicknesses of approximately 0.5 and 0.8 μm were obtained, respectively.

Across all conditions, photoresist 2 consistently yielded thinner films than photoresist 1 under identical spin-coating parameters. This behavior is likely due to the higher DMAEMA content in photoresist 2, which presumably reduces viscosity.

To evaluate feature resolution as a function of laser intensity, 0.8 μm-thick films prepared using photoresist 1 were subjected to film-based MPL. In these experiments, four parallel lines measuring 50 μm in length and spaced 10 μm apart were fabricated at a constant writing speed of 5 mm s^{-1} using three different objective lenses (Plan-Apochromat, Zeiss, Germany) and analyzed via scanning electron microscopy (SEM). The lenses used were (1) 40x/0.95 (maximum FOV = 625 μm), (2) 20x/0.8 (maximum FOV = 1250 μm), and (3) 10x/0.45 (maximum FOV = 2500 μm).

The average feature widths determined for each case by the four lines are presented as dots in Figure 2B, with representative SEM images of the printed lines shown in Figure 2C. Both the graph and SEM images illustrate that sub-micron line widths are achievable with all three objective lenses. Additionally, by adjusting the laser intensity at the focal plane, the line widths can be precisely altered within the micrometer range.

The growth behavior of the line width can generally be described by $w = 2r\sqrt{2\ln(I/I_{th})}$,[52] although w typically represents the voxel width. However, since MPL is initiated upon threshold excitation, the feature width may closely approximate that of a single voxel under constant process parameters.[53] Thus, w can refer to the feature width, with I representing the laser peak intensity used for structuring and I_{th} as the threshold laser peak intensity. Additionally, the beam radius r can be expressed as $0.61\lambda/NA$, where λ is the central wavelength of the laser. The laser peak intensity can be calculated as $I = 2(TP_a)/(\pi r^2 p_R \tau)$, where T is the transmission of the objective lens, P_a is the average laser power, p_R is the repetition rate, and τ is the pulse duration. Further details on process parameters used to calculate feature resolution are provided in the Supporting Information.

As shown in Figure 2B, applying the theoretical approach to fit the experimental data yields accurate results, supporting two key assumptions: (I) the theoretical model describing feature resolution in traditional MPL is also valid for film-based MPL, and (II) diluting the photoresist with distilled water to achieve thinner films does not significantly impact the printing process.

The threshold laser peak intensity at a writing speed of 5 mm s^{-1} was approximately 0.15 TW cm^{-2}, as determined using the camera in the MPL setup (see Figure 1). However, the smallest solid lines that remained after the development process could be fabricated at slightly higher peak intensity, around 0.19 TW cm^{-2}. The minimum line widths achieved were approximately 250 nm ± 12 nm (NA = 0.95), 350 ± 11 nm (NA = 0.8), and 500 nm ± 23 nm (NA = 0.45), respectively.

Particularly near the polymerization threshold, some deviation was observed, mainly due to the lines tilting slightly during the development process. At higher laser intensities, this deviation became negligible, as the feature size was highly consistent. For all sets of lines produced, the axial dimension–approximating the length of a single voxel–exceeded the thickness of the film, as theoretically demonstrated in the Supporting Information.

Notably, MPL was initiated at the same threshold intensity when using photoresist 2, suggesting similar feature resolution characteristics, as evidenced by the printed metasurfaces discussed later. The identical threshold intensity for both photoresists can be attributed to their similar composition, particularly the use of the same photoinitiator, which is the primary factor influencing the efficiency of MPL.[54]

3. Capabilities of Printing Electromagnetic Surface Structures Via Film-Based MPL

3.1. THz Metasurfaces Via Silver Split-Ring Resonators

To demonstrate the potential of film-based MPL in fabricating electromagnetic surface structures, the printing of a prototypical metasurface consisting of split-ring resonators (SRRs) was targeted, designed for operation at THz frequencies. At the same time, this study simultaneously highlights the inherent flexibility of MPL, particularly for the use of post-processing techniques such as SESP. The thickness of the SRRs was defined by the film itself, while other SRR dimensions are depicted in **Figure 3A**. SRRs were chosen due to their proven versatility across various applications,[55–57] making them an excellent candidate for showcasing the capabilities of film-based MPL. These structures are particularly notable for supporting distinct electric or magnetic resonances, depending on the orientation of the meta-atoms relative to the incident excitation (direction and polarization).[58]

Utilizing dielectric SRRs for THz applications would require materials with a very high refractive index (a property polymers do not inherently provide) so as to achieve strong displacement currents. Nonetheless, the incorporation of 30% DMAEMA as an organic monomer into the photoresist 2 enabled SESP, allowing a thin metallization layer to coat the polymer structures. This approach enables the fabrication of metallized SRRs (see Figure 3A). Consequently, strong conduction currents can be fostered by the meta-atoms resulting in a resonant response for the metasurface.

As a proof of concept for film-based MPL, an SRR-metasurface with a minimum feature size of approximately 1 μm was fabricated. To achieve this, a 1-μm-thick film was produced via spin-coating at 1500 rpm using photoresist 2. Polymeric SRRs were then printed in single arrays with a spacing of p = 10 μm between them, using a 10x objective lens (NA = 0.45). A total of 144 arrays were assembled into a 12x12 grid, with each array written within a 1 mm × 1 mm effective field of view (FOV) at a scanning speed of 5 mm s^{-1} and focal intensity of approximately 0.2 TW/cm^2, ultimately covering an area of approximately 1.2 cm x 1.2 cm (see Figure 3A). The specific SRR geometry was

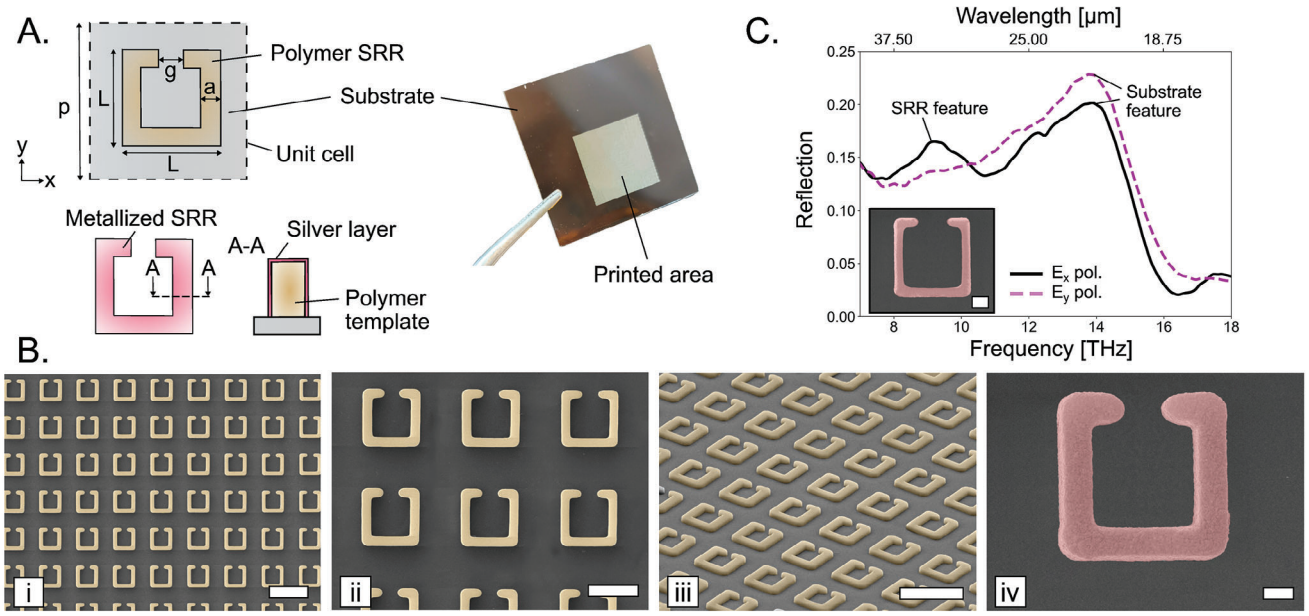

Figure 3. Silver SRRs printed by film-based MPL. A) The photo shows a metasurface (1.2 cm x 1.2 cm) printed by film-based MPL. The area contained polymer SRRs designed as schematically shown in the upper left corner. These polymer SRRs were used as templates that were further processed by SESP to selectively cover the structures with silver nanoparticles. B) SEM images at different magnifications (i-iii) show polymer SRRs, highlighted in yellow. In case (iv), a metalized SRR, highlighted in red, is shown after SESP. The scale bar is 10 μm (i, iii), 5 μm (ii), and 1 μm (iv). C) The graph illustrates the response of a SRR-metasurface on soda-lime glass substrate analyzed using FTIR. The cropped SEM image provides a detailed view of one of the corresponding SRR, with a scale bar indicating 1 μm.

printed by scanning the beam with the galvo scanner. Notably, the effective FOV of the objective lens was reduced compared to its specifications due to optical aberrations when scanning the laser beam with the galvo scanner. However, it remained larger than the FOV of oil-immersion objective lenses, which are typically used in traditional MPL for fabricating structures with similar features, particularly those targeting a structure height at such small scales. This advancement, coupled with the ability to fabricate each structure in a single exposure, enabled the entire area to be fabricated in approximately 120 min, accounting for device delays and stage movements.

Following the film-based MPL process, the SRRs underwent SESP to selectively coat the structures with silver nanoparticles. The SESP procedure was based on the method described in Ref. [37], with the plating step repeated twice instead of five times. This adjustment is expected to result in a silver layer approximately 50 nm thick, ensuring that the SRRs functioned as efficient conductors preventing field penetration into the polymeric templates.

A detailed view of the printed SRRs is presented through the SEM images in Figure 3B. For enhanced visualization, the polymer SRRs are highlighted in yellow (see Figure 3B, i–iii). Overall, the SRRs exhibited high printing quality, with uniform geometry, and consistent height across the array. Precise positioning was achieved within each individual array; however, some non-consistent stitching errors were observed between arrays, attributed to the precision limits of the axis system (see Supporting Information). Furthermore, the quality of single SRRs remained largely unaffected by the SESP process, as shown in Figure 3B (iv), where a metallized SRR is highlighted in red. The selectivity of the process is also evident, with silver nanoparticles confined to the surface of the SRR and absent from the surrounding substrate, as further demonstrated by energy-dispersive X-ray (EDX) analysis presented in the Supporting Information.

To further validate the functionality of these metasurfaces in the THz electromagnetic spectrum, film-based MPL and SESP were again employed to fabricate another metasurface with slightly modified SRR dimensions while maintaining the same total area. This metasurface was subsequently analyzed using Fourier-transform infrared (FTIR) spectroscopy. In this case, the target SRR dimensions were set as follows: $W = L = 5$ μm, $g = 2$ μm, $w = 0.5$ μm, $p = 10$ μm, and a SRR height of 600 nm.

For improved handling during post-processing and optical analysis, a photosensitive film was processed this time on standard microscope slide made of soda-lime glass. In this case, a film with a thickness of 600 nm was achieved by using photoresist 2 and applying a spin-coating process at an angular velocity of 4500 rpm. The minimum feature size of $w = 0.5$ μm was obtained by setting the laser peak intensity to approximately 0.19 TW cm^{-2} at a writing speed of 5 mm s^{-1}. The specific SRR geometry was realized by scanning the beam with the galvo scanner.

FTIR measurements were conducted in reflection mode in the range of 7–18 THz with a measurement resolution of 4 cm^{-1} and further details presented in the Supporting Information. The THz beam had a diameter of approximately 1 cm and was directed onto the SRRs at incident and reflected angles of 13° relative to the *yz* incidence plane (see coordinate system in

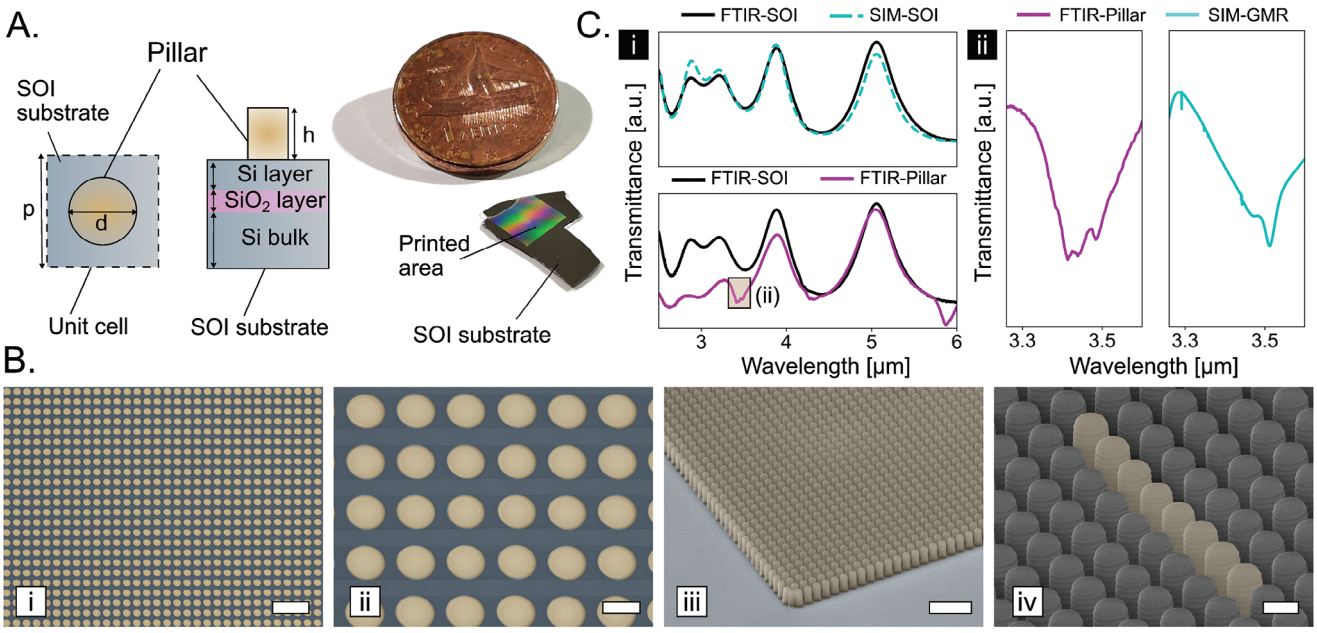

Figure 4. Pillars on SOI substrate fabricated by film-based MPL. A) The schematic illustrates the disk structures on top of a SOI wafer, including the dimensions of the pillar and the unit cell. The photo depicts a printed surface (5 mm x 5 mm) on an SOI substrate in comparison to the size of a 1-eurocent coin. B) SEM images at different magnifications (i-iii) display the pillars, highlighted in yellow, on the SOI wafer, which is highlighted in blue-gray. The scale bars measure 10 μm (i, iii) and 2 μm (ii, iv). C) The graph shows the response of the processed SOI device as analyzed by FTIR. The results are supported by simulations.

Figure 3A). Two polarizers were employed to excite and analyze the fabricated SRRs under the two orthogonal linear polarizations: Transverse Electric (TE), which corresponds to nonzero E_x component, and Transverse Magnetic (TM) which corresponds to nonzero E_y (and E_z). The measured response of the metasurface for both linear polarization states as well a detailed view on one of the corresponding unit cells is depicted in Figure 3C. As anticipated, the fundamental SRR resonance was observed only with the E_x polarization, resulting in a spectral feature (reflection peak) at approximately 9 THz. However, both curves also exhibit a pronounced spectral feature around 14 THz, which can be attributed to the material properties of the soda-lime glass substrate (see Supporting Information). Taking into account SRR dimensions and material properties of the substrate, full-wave simulations closely matched the FTIR measurements, as presented in the Supporting Information.

3.2. Mid-IR Metasurfaces Via Polymer Pillars on SOI Substrates

A second case study was conducted to further demonstrate the potential of film-based MPL, focusing on dielectric surface structures designed to provide a corrugation at the surface of an SOI substrate. More specifically, these structures typically enable the coupling of incident electromagnetic waves to leaky photonic modes guided mainly within the silicon device layer of the substrate. Thanks to its strong frequency selectivity, this phenomenon, commonly referred to as guided-mode resonances (GMRs), is particularly interesting for applications such as spectroscopy,[59] sensing or short-cavity lasing.[60] In this context, the conditions for the appearance of GMRs can be described by the following equation:

$$\left|\left(\sin\theta\cos\phi - \frac{m\lambda_{\text{res}}}{p}\right)\mathbf{x} + \left(\sin\theta\sin\phi - \frac{n\lambda_{\text{res}}}{p}\right)\mathbf{y}\right| = n_{\text{eff}} \quad (1)$$

Here, θ and ϕ represent the angles of incidence and polarization of a plane wave, respectively, while m and n are integers. λ_{res} refers to the wavelengths of the resonance, and n_{eff} denotes the effective index of the propagating mode.[61] However, when the incident electromagnetic wave is orthogonal to the substrate surface, the equation can be simplified to: $\sqrt{m^2+n^2}\lambda_{\text{res}} = pn_{\text{eff}}$.

To practically excite the GMRs, polymer pillars were fabricated on a commercially available, double-polished SOI substrate, as schematically shown in **Figure 4A**. The SOI substrate was specified by a silicon device layer (Si), buried silica oxide (SiO_2), and bulk silicon substrate (BSi), with thicknesses of $t_{\text{Si}} = 2.2$ μm, $t_{\text{SiO}_2} = 1.09$ μm, and $t_{\text{BSi}} = 725$ μm, respectively.[62] The designed periodicity, diameter, and height of the polymer pillars were $p = 3$ μm, $d = 1.8$ μm, and $h = 5.8$ μm, respectively.

To fabricate these pillars, a photosensitive film was spin-coated onto an SOI substrate at 1900 rpm using photoresist 1. The spin-coating parameters were selected based on those optimized in earlier experiments conducted on coverslips. Subsequently, the film was processed using film-based MPL with a 10x objective lens (NA = 0.45), enabling the creation of a 5 mm x 5 mm area (see photo in Figure 4A). The total fabrication time, including device delays and stage movements, was approximately 55 min. Notably, for the experiment, the optical setup illustrated in Figure 1 remained effective and did not require optimization, even though

the LED could not be used due to the optical properties of the substrate. Instead, the back reflection of the SOI substrate was used to identify the substrate's surface with the camera.

The large area comprised individual 0.5 mm × 0.5 mm arrays stitched together, while each array contained approximately 27 500 pillars. This smaller array size, compared to those used in SRR experiments, was chosen to minimize potential structural imperfections arising from interactions between incident and reflected laser radiation at larger scanning angles. Within individual arrays, each pillar was fabricated by exposing the film to a laser peak intensity of approximately 0.37 TW cm^{-2} for 0.4 ms at precise locations, resulting in features with a width of approximately 1.8 µm. The fabrication parameters were derived from previous studies, ensuring the same number of laser pulses per exposed position as those used in experiments that produced 50 µm-long lines at a writing speed of 5 mm s^{-1} (see Figure 1B).

The printed pillars are shown in Figure 4B. The arrays exhibited high printing quality, with no defects between the pillars that might have resulted from interactions between reflected laser radiation and material pre-excited below the polymerization threshold. However, structural imperfections along the pillars' vertical axes resulted from interference between incident and reflected laser radiation, modulating the printed structure at specific axial positions according to the equation $k\lambda/(4n)$, where k is a positive integer, λ the central wavelength of the laser radiation, and n is the refractive index of the photoresist.

To further investigate the excitation of GMRs, the fabricated sample was characterized in the mid-IR range using FTIR in transmission mode (2–20 µm, resolution of 2 cm^{-1}). Measurements were conducted using a 15x IR objective lens (NA = 0.4) and a fixed aperture of 0.9 mm, focusing on a single printed array to avoid potential errors of stitched areas (detailed in the Supporting Information) that could affect the GMR detection.

FTIR analysis was initially performed on the bare SOI substrate, followed by the evaluation of a printed array. The corresponding results for both cases are shown in Figure 4C(i). The transmission spectrum was further compared with simulations conducted using rigorous coupled-wave analysis (RCWA),[63,64] starting with the bare SOI substrate. For simplicity in the RCWA analysis, normal incidence of the electromagnetic wave on the substrate surface was assumed. The refractive indices and dispersion parameters for silicon and silica used in the simulations were sourced from refs. [65, 66].

The good agreement between the experimental and simulated results for the bare SOI substrate validates the accuracy of the silicon device dimensions and and the SiO_2 buffer layer thickness. Consequently, RCWA analysis can also be reliably applied to printed pillars on the SOI substrate.

Examining the spectral response of the printed pillars (see Figure 4C(i)), a prominent transmittance dip is observed at 5.8 µm. This dip, however, is not attributed to a GMR but rather to the absorption band of the photoresist.[67] Nonetheless, GMR excitation was identified within the spectral region around 3.5 µm, which is highlighted in yellow in Figure 4C(i) and detailed further in Figure 4C (ii) in the graph on the left-hand side. Notably, RCWA simulations confirmed the correlation of the experimentally observed resonant feature with GMRs. These simulations were performed with a spectral resolution of 0.1 nm, incorporating the resist's refractive index, assumed to be $n = 1.45\text{-}j0.013$.[68]

In the simulated spectrum (see Figure 4C (ii), graph on the right-hand side), a few sharp resonances were observed, attributed to GMRs. The narrow linewidth of these resonances is a consequence of the low refractive index of the polymer, which is significantly lower than that of the guiding layer. This results in weak index modulation and minimal radiative losses. In contrast, sharp resonances were absent in the experimental data, primarily due to factors that broaden the resonance. One possible factor is the angular content of the probe beam used in FTIR analysis; as indicated by the aforementioned equation, GMRs are highly sensitive to the angle of incidence. However, imperfections in the pillars' geometry, particularly their wavy cross-section, are likely the primary contributors to resonance broadening and other deviations from the simulated results, such as a slight blue shift.

While the height of the pillars in a single array should theoretically be uniform–profilometer measurements of polymerized films over the same length as the array did not show significant deviations beyond the axial resolution of the profilometer–the wavy contour makes the structures more susceptible to slight tilts during development, when the unexposed material is removed (see Supporting Information). These small geometric variations compromise overall uniformity.

Additionally, the interference of partially reflected laser radiation with the incident beam occurs only within a specific length due to the focused nature of the laser. As a result, the upper parts of the structures are often more polymerized than the lower parts, which, in turn, causes the effective diameter to vary along the length of a single structure (see Supporting Information) and, consequently, the effective refractive index as well. Nevertheless, the imperfections resulting from the wavy-shaped cross-section are generally uniform, as the optical properties measured by FTIR for the arrays produced at each corner of the sample remained similar. (see Supporting Information, Figure S3).

As such, despite the resonance broadening and a slight blue shift relative to the simulated spectrum, the resonant feature can be associated with GMRs induced by the printed pillars. These findings further underscore the versatility of film-based MPL, highlighting its potential for applications across various spectral regimes and its capability for large-area printing, even on challenging substrates.

3.3. Further Potential of Film-Based MPL for Printing Surface Structures

Two additional proof-of-concept studies were conducted to further explore the potential of film-based MPL for fabricating surface structures. These studies aimed to demonstrate the versatility of the technique, showcasing its ability to produce surface structures with (1) modified material properties, (2) enhanced feature resolution, and (3) extended printing capabilities beyond the creation of planar 2D structures.

Focusing on electromagnetic surface structures, MPL printing processes typically rely on polymers. However, their applications, particularly in photonics, are often constrained by the material's refractive index. To overcome these limitations, specific approaches, such as SESP, allow for the selective metallization of surface structures, enabling effective manipulation of electromagnetic radiation at lower frequencies. Despite their

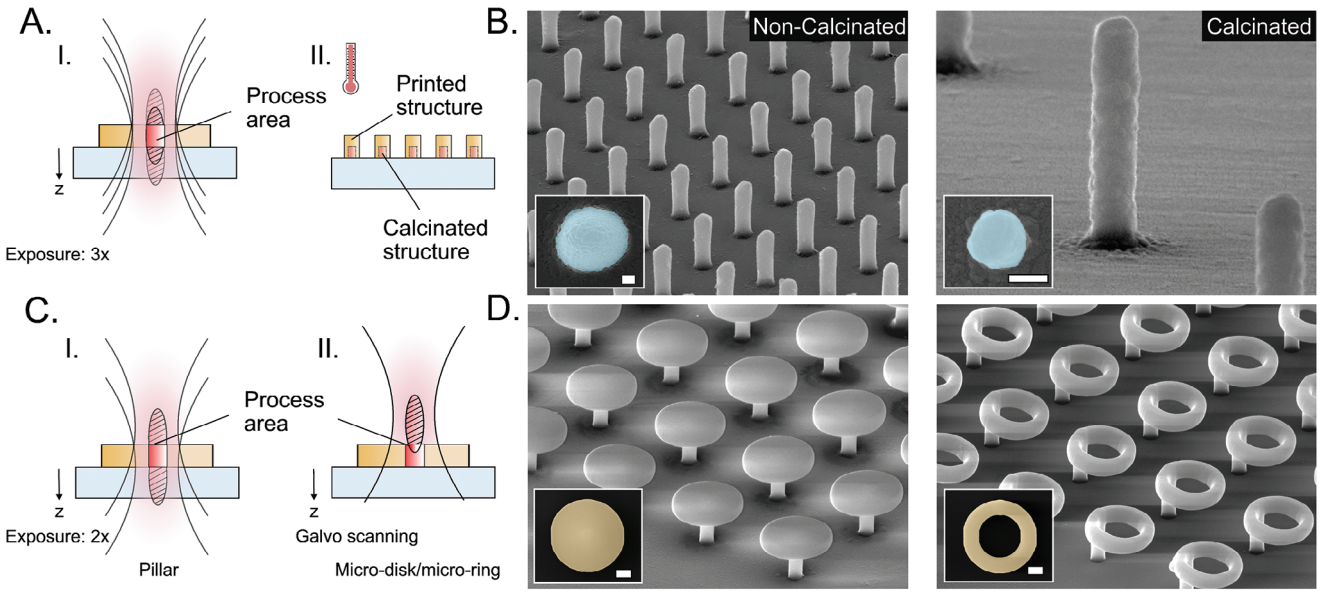

Figure 5. Feature reduction, inorganic structures and structures with 2.5D complexities. A) Schematic illustration of film-based MPL for fabricating pillars in a TiO_2-based photoresist, followed by post-processing via calcination. B) Pillars produced directly after film-based MPL and the resulting TiO_2 pillars post-calcination. The scale bars in the insets are 200 nm. C) Principle for printing structures with 2.5D complexities using film-based MPL. D) SEM images of 2.5D micro-disks and micro-rings captured at a 45° tilt view. The scale bars in the insets are 1 µm.

advantages, metals become less effective at higher frequencies, such as those in the visible and near-infrared spectra, due to significant ohmic losses. In such cases, dielectric materials are preferred for their superior performance.

In this context, film-based MPL facilitates the efficient fabrication of dielectric structures using an organic-inorganic hybrid photoresist with adjustable inorganic content. Post-processing through calcination can remove the organic component via heat treatment,[69] resulting in a purely inorganic structure (see **Figure** 5A). Interestingly, this process also induces volumetric shrinkage, enhancing feature resolution and potentially improving the suitability of these structures for metasurface applications in the visible and near-infrared spectra.

To demonstrate this approach, a hybrid photoresist incorporating titanium dioxide (TiO_2) as the inorganic component was synthesized, as detailed in ref. [70]. The resist was not diluted and spin-coated onto a quartz substrate at 4000 rpm, resulting in a film thickness of approximately 4 µm. Following spin-coating, pillars separated by 5 µm were printed using a 20x objective lens (NA = 0.8) with a laser peak intensity of about 0.25 TW cm^{-2}. In this case, three exposures separated by 1.5 µm along the z-axis, each lasting 0.4 ms, were applied. This approach aimed to achieve high lateral resolution while ensuring that the entire film thickness was exposed, as the theoretical voxel length was smaller than the film thickness (see Supporting Information). Calcination was then performed following the protocol described in Ref. [70].

The pillars, both before and after calcination, are shown in Figure 5B. Remarkably, no structural delamination was observed post-calcination, preserving the periodicity of the structures. Initially, each pillar measured approximately 800 nm in diameter and 4 µm in height. After calcination, the features shrank laterally to around 250 nm and axially to 1.25 µm, corresponding to a consistent volumetric shrinkage factor of about 3.2, while maintaining an aspect ratio of 1:5. Notably, even higher aspect ratios might be achievable, as the highest aspect ratio observed for the pillars prior to calcination was 1:10 (see Supporting Information).

Furthermore, to explore film-based MPL for applications beyond 2D, the concept illustrated in Figure 5C was used to fabricate 2.5D structures. In this process, a 3 µm-thick film was spin-coated at 3000 rpm onto standard coverslips using photoresist 1. Subsequently, multiple exposure events produced micro-disks and micro-rings, each connected by a small pillar that elevates the structure from the substrate. Fabrication was conducted in an array format: each pillar was initially created by localized resist exposure, followed by the specific geometry atop, achieved by deflecting the laser beam with a galvo scanner.

Each pillar was fabricated by two exposures of the resist at axial positions separated by 1.5 µm, with each exposure lasting 0.4 ms. This process resulted in pillars approximately 900 nm in diameter. The stage was then shifted further downward along the axial direction, enabling partial voxel regions to be used for subsequent printing. During this step, circular scans of the resist were executed at a writing speed of 5 mm s^{-1}. The diameter of each circular scan progressively decreased, with a spacing of 0.2 µm between successive circles. Repeating this decrement for 20 cycles resulted in a fully polymerized disk with a total diameter of 4.5 µm and a thickness of 1 µm. In contrast, micro-ring structures were printed by performing two circular scans per ring, spaced 0.2 µm apart. This process produced rings with radial and axial feature sizes of approximately 1 µm.

The resulting 2.5D micro-disks and micro-rings are shown in Figure 5D, with high-magnification SEM images of the side views provided in the Supporting Information. For all experiments, the 40x objective lens (NA = 0.95) was employed at a peak intensity of approximately 0.35 TW cm^{-2}.

4. Discussion and Conclusion

The research presented in this work introduced an optimized approach for efficiently printing surface structures using MPL, with a particular focus on electromagnetic surface structures. The optimization was based on employing a thin film of photosensitive material instead of the conventional droplet-shaped volume. This simple modification of the MPL process, referred to here as film-based MPL, significantly accelerated the fabrication process by reducing the required number of exposure events–ideally down to a single exposure event per structure while maintaining high-resolution printing capabilities even with objective lenses having NAs below 1.

The key to these improvements was to minimize the influence of MPL's axial resolution, represented by the voxel lengths. As a result, by limiting the film thickness to a few µm or even sub-µm, film-based MPL was particularly well-suited for large-area structuring of planar 2D structures, where laser peak intensity can be precisely tuned to match the desired feature size of a single structure, thanks to the nonlinear characteristics of MPL. Large-area printing was further supported since film-based MPL provided robustness against sample tilt errors.

To demonstrate the potential of film-based MPL, the fabrication process focused on metasurfaces relevant to mid-IR and THz spectral applications, as these spectral ranges align well with MPL's resolution capabilities for manufacturing suitable structures. Thin films of appropriate thickness were primarily produced by spin-coating two different hybrid photoresists diluted with distilled water. Importantly, this dilution did not compromise MPL processability, and the spin-coating process enabled the generation of films with uniform thickness.

The feature resolution achievable with film-based MPL was evaluated using dry objective lenses with three different NAs. Using a 40x objective lens (NA = 0.95), a minimum lateral feature resolution of approximately 250 nm was achieved. Remarkably, even with a 10x objective lens (NA = 0.45), sub-micron features were successfully fabricated, achieving minimum feature sizes around 500 nm–adequate for realizing mid-IR and THz metasurfaces.

Rapid large-area fabrication at scales of cm^2 and mm^2 was demonstrated using the 10 × objective lens. Specifically, SRRs were successfully printed on a 1.2 cm × 1.2 cm area within 120 min, and pillars were fabricated on a 5 mm × 5 mm area within 55 min. The SRRs exhibited a minimum feature size of 550 nm with a height of 600 nm, while the pillars displayed diameters and heights of 1.8 and 5.8 µm, respectively, with a minimum spacing of 1 µm. Achieving these dimensions within such short timeframes–particularly with an objective lens with NA of 0.45–presents significant challenges for traditional MPL, where structure printing typically relies on a layer-by-layer approach.

Alongside advancements in fabrication speed compared to traditional MPL, this study further demonstrated the versatility of film-based MPL in creating diverse surface structures with enhanced flexibility. For example, film-based MPL could be combined with SESP, enabling the metallization of SRRs across a large area for THz applications. Additionally, pillars were fabricated on an SOI substrate to manipulate mid-IR electromagnetic radiation. Here, the use of a thin film addressed challenges in large-area manufacturing, particularly those posed by the substrate–s optical properties, which usually complicate accurate interface detection. Notably, these two cases are just examples of the potential applications of film-based MPL. Functionalization of structures may also be achievable through various other approaches.[71] Furthermore, MPL supports the fabrication of structures on a wide range of substrates, including their transfer onto complex surfaces with arbitrary curvature.[72]

In conclusion, while the primary strength of MPL lies in its maskless 3D printing capabilities, this study demonstrates that, with a carefully optimized printing process, MPL can also be highly effective for 2D printing jobs. Notably, it offers flexibility in structural geometry and orientation, as detailed in the Supporting Information. Additionally, film-based MPL even facilitates 2.5D structuring, which may enable the isolation of planar electromagnetic surface structures from the substrate, thereby reducing radiation leakage and enhancing resonant electromagnetic fields. Nevertheless, it is worth noting that achieving 2.5D structuring over larger areas introduces additional challenges, particularly due to the higher precision required for stage movement and interface detection. Despite these challenges, film-based MPL offers greater flexibility and improved speed compared to the traditional MPL approach.

With this, the study demonstrated that MPL can perform 2D, 2.5D, and 3D structuring within a single device. This versatility offers significant advantages over conventional lithographic techniques, particularly since MPL does not require a vacuum atmosphere or exposure masks. Moreover, based on the results of this study, considering fabrication time, achievable dimensions, and minimum feature resolution, film-based MPL is emerging as a viable competitor to commercially available DLW systems using CW diode lasers at 375 nm/405 nm, especially those operating in high-resolution modes.[26,27] Additionally, it offers greater manufacturing capabilities, which are far from trivial to achieve using DLW with CW lasers or any other comparable lithographic technique.

For example, film-based MPL enables the fabrication of densely-packed, high-aspect-ratio structures, with the maximum aspect ratio presented in this study being 1:10. In addition, film-based MPL even allows for the realization of 2.5D structures, as mentioned earlier, with features theoretically compatible with mid-IR applications (see Figure 5C).

Interestingly, as MPL itself is an emerging technology, film-based MPL still offers substantial room for optimization, as outlined below. As such, film-based MPL may further establish MPL as an advanced and superior fabrication tool compared to conventional DLW for future flat optical and photonic device manufacturing, including electromagnetic surfaces, extending beyond mid-IR to THz frequencies and covering even broader spectral regimes.

Specifically, the fabrication speed of film-based MPL can be further enhanced through photosensitive materials with improved sensitivity[46,73] as well as parallelization[44,45,74,75] or projection writing techniques;[43,76] these approaches are direct outcomes of recent advancements in MPL printing detailed in refs. [29,42]. The use of diffractive optical elements or spatial light modulators may also facilitate beam profile shaping, such as generating Bessel beams, which could be advantageous for fabricating high-resolution structures with even higher aspect ratios than 1:10. Additionally, dynamic voxel refinement–achievable

with devices such as acousto-optical modulators or digital mirror devices–enables grayscale-based printing,[31,43] allowing for greater precision in structural features and the fabrication of surfaces with gradient-index structures.

Furthermore, although the feature resolution in this work was limited to 250 nm–comparable to the physical limit achievable with diode laser-based DLW–MPL offers several options for further enhancement, making it highly versatile for surface structuring. For instance, feature resolution can be improved through etching[77] or, as demonstrated, via calcination,[69] though such post-processing techniques could also be applied to other DLW processes.

Additionally, while the experiments in this work were conducted at 780 nm, modern fs-oscillators now allow for wavelength-independent MPL, enabling processing at various wavelengths.[78] This, in turn, may facilitate tighter focusing to reduce the feature size. Even more interestingly, feature resolution may be further enhanced using annihilation processes [79] or stimulated emission depletion,[80,81] which not only enable higher feature resolution but also significantly reduce the spacing between structures–a critical aspect in CW laser-based DLW due to scattering of laser radiation into surrounding areas of the material.

While annihilation processes and stimulated emission depletion techniques typically face challenges in efficient application to MPL for 3D printing, they may be particularly well-suited for integration with film-based MPL, especially for 2D and even 2.5D structuring, where ideally only a single or two planes of the photosensitive material are exposed, respectively. Furthermore, these methods can be effectively combined with etching and calcination to optimize results further.

Notably, calcination is particularly promising–not only for enhancing feature resolution but also for enabling the fabrication of structures from various inorganic materials. Interestingly, for 3D structures, calcination often causes delamination from substrates due to thermal stress.[70,82] However, in this work, thermal stress did not affect the printed pillars, thus preserving their periodic arrangement. Although the relationship between thermal stress-induced delamination and critical structural parameters requires further investigation, these findings suggest a pathway for large-area fabrication of dielectric surface structures via film-based MPL, potentially enabling the realization of printed NIR and even VIS metasurfaces with (deeply) subwavelength features.

Finally, while this study primarily focused on manufacturing electromagnetic surface structures, the approach is not limited to this application alone. The capabilities film-based MPL offers can be highly valuable for diverse fields such as biomimetic,[83] optics,[84] and biomedicine,[6] where future research on 2D structures can inspire 2.5D and 3D designs, all achievable with a single technology–MPL–and, consequently, a single device. In this context, film-based MPL proves useful not only for rapid prototyping but also for creating blueprints and real-world applications.

Supporting Information

Supporting Information is available from the Wiley Online Library or from the author.

Acknowledgements

This research was supported by the Marie Sklodowska-Curie Actions, under grant agreement No. 101059253, as part of the European Union's Horizon Europe research and innovation programme. It also received support from a Feodor Lynen Postdoctoral Fellowship awarded by the Alexander von Humboldt Foundation. Additionally, this work was partially supported by the European Union through project FABulous (HORIZON-CL4-2022-TWIN-TRANSITION-01-02, GA:101091644). D.C.Z. acknowledges the support by the project ECS00000024 "Ecosistemi dell'Innovazione"-Rome Technopole of the Italian Ministry of University and Research, public call n. 3277, PNRR-Mission 4, Component 2, Investment 1.5, financed by the European Union, Next GenerationEU (CUP: B83C22002890005). The research project was co-funded by the Stavros Niarchos Foundation (SNF) and the Hellenic Foundation for Research and Innovation (H.F.R.I.) under the 5th Call of "Science and Society" Action – "Always Strive for Excellence – Theodore Papazoglou" (Project Number: 9578). G.Z. acknowledges the "Universities' Excellence Initiative" programme by the Ministry of Education, Science and Sports of the Republic of Lithuania under the agreement with the Research Council of Lithuania (project No. S-AUEI-23-6). G.Z. also acknowledges support from the Vilnius University Foundation through the 2024 co-funding competition award. The authors would like to thank Mr. Andreas Lemonis for his technical support with MPL software development, Mr. Thansis Kostopolous for his assistance with film thickness measurements, and Mrs. Aleka Manousaki for her support in recording the SEM images.

Conflict of Interest

The authors declare no conflict of interest.

Author Contributions

The study concept was conceived by G.Z., O.T., and M.F. Photosensitive materials were synthesized by G.Z., S.P., and A.C. Experiments related to film-based multi-photon lithography (MPL) were conducted by G.Z., S.P., and A.C., with final data preparation and analysis performed by G.Z. Designs for electromagnetic surface structures and simulations were proposed and performed, respectively, by O.T. and D.C.Z. Fourier-transform interferometry spectroscopy was carried out by G.Z. and G.K.

G.Z. led the manuscript preparation, with support from O.T. and D.C.Z. All authors reviewed and commented on the manuscript and contributed to discussions of the data. The project was supervised by G.Z. and O.T.

Data Availability Statement

The data that support the findings of this study are available from the corresponding author upon reasonable request.

Keywords

direct laser writing, metasurfaces, multi-photon lithography, surface structures, thin-films

Received: December 16, 2024
Revised: January 25, 2025
Published online:

[1] S. N. Gorb, *Functional Surfaces in Biology*, Springer Netherlands, Dordrecht **2009**.

[2] B. Bhushan, *Philos. Trans. R. Soc., A* **2009**, *367*, 1445.
[3] G. Zyla, A. Kovalev, M. Grafen, E. L. Gurevich, C. Esen, A. Ostendorf, S. Gorb, *Sci. Rep.* **2017**, *7*, 17622.
[4] E. Arzt, H. Quan, R. M. McMeeking, R. Hensel, *Prog. Mater. Sci.* **2021**, *120*, 100823.
[5] E. Stratakis, J. Bonse, J. Heitz, J. Siegel, G. D. Tsibidis, E. Skoulas, A. Papadopoulos, A. Mimidis, A. C. Joel, P. Comanns, J. Krüger, C. Florian, Y. Fuentes-Edfuf, J. Solis, W. Baumgartner, *Mater. Sci. Eng.: R: Reports* **2020**, *141*, 100562.
[6] G. Flamourakis, Q. Dong, D. Kromm, S. Teurlings, J. van Haren, T. Allertz, H. Smeenk, F. M. S. de Vrij, R. P. Tas, C. S. Smith, D. Brinks, A. Accardo, *Adv. Funct. Mater. n/a*, 2409451.
[7] E. Skoulas, A. C. Tasolamprou, G. Kenanakis, E. Stratakis, *Appl. Surf. Sci.* **2021**, *541*, 148470.
[8] M. Lee, G. Kim, Y. Jung, K. R. Pyun, J. Lee, B.-W. Kim, S. H. Ko, *Light Sci Appl* **2023**, *12*, 134.
[9] C. M. Soukoulis, M. Wegener, *Nature Photon* **2011**, *5*, 523.
[10] R. Sokhoyan, P. Thureja, J. Sisler, M. Grajower, K. Shayegan, E. Feigenbaum, S. Elhadj, H. A. Atwater, *Nanophotonics* **2023**, *12*, 239.
[11] K. Du, H. Barkaoui, X. Zhang, L. Jin, Q. Song, S. Xiao, *Nanophotonics* **2022**, *11*, 1761.
[12] T. Pertsch, S. Xiao, A. Majumdar, G. Li, *Photon. Res., PRJ* **2023**, *11*, OMFA1.
[13] O. Tsilipakos, M. Kafesaki, E. N. Economou, C. M. Soukoulis, T. Koschny, *Adv. Opt. Mater.* **2020**, *8*, 2000942.
[14] K. Ou, H. Wan, G. Wang, J. Zhu, S. Dong, T. He, H. Yang, Z. Wei, Z. Wang, X. Cheng, *Nanomaterials* **2023**, *13*, 1235.
[15] W. T. Chen, A. Y. Zhu, F. Capasso, *Nat. Rev. Mater.* **2020**, *5*, 604.
[16] D. N. Neshev, A. E. Miroshnichenko, *Nat. Photon.* **2023**, *17*, 26.
[17] M. Kadic, G. W. Milton, M. van Hecke, M. Wegener, *Nat. Rev. Phys.* **2019**, *1*, 198.
[18] X. Zhao, Z. Sun, L. Zhang, Z. Wang, R. Xie, J. Zhao, R. You, Z. You, *Adv. Dev. Instrument.* **2022**, *2022*.
[19] J. Hu, S. Bandyopadhyay, Y.-h. Liu, L.-y. Shao, *Front. Phys.* **2021**, *8*.
[20] Y. Kivshar, *Natl. Sci. Rev.* **2018**, *5*, 144.
[21] T. Pertsch, Y. Kivshar, *MRS Bull.* **2020**, *45*, 210.
[22] W. Su, P. Cai, J. Darkwa, M. Hu, G. Kokogiannakis, C. Xu, L. Wang, *Appl. Therm. Eng.* **2023**, *235*, 121305.
[23] S. Shrestha, A. C. Overvig, M. Lu, A. Stein, N. Yu, *Light Sci. Appl.* **2018**, *7*, 85.
[24] B. Leng, Y. Zhang, D. P. Tsai, S. Xiao, *Light: Advanced Manufacturing* **2024**, *5*, n/a.
[25] X. Xiao, Y. Zhao, X. Ye, C. Chen, X. Lu, Y. Rong, J. Deng, G. Li, S. Zhu, T. Li, *Light Sci. Appl.* **2022**, *11*, 323.
[26] Heidelberg Instruments, https://heidelberg-instruments.com/product/dwl-2000-4000-laser-lithography-systems, DWL 2000 GS/DWL 4000 GS (accessed: June 2024).
[27] Heidelberg Instruments, https://heidelberg-instruments.com/product/dwl-66-laser-lithography-system, DWL 66+ (accessed: June 2024).
[28] H. Wang, W. Zhang, D. Ladika, H. Yu, D. Gailevičius, H. Wang, C.-F. Pan, P. N. S. Nair, Y. Ke, T. Mori, J. Y. E. Chan, Q. Ruan, M. Farsari, M. Malinauskas, S. Juodkazis, M. Gu, J. K. W. Yang, *Adv. Funct. Mater.* *33*, 2214211.
[29] G. Zyla, M. Farsari, *Laser Photonics Rev.* **2024**, *18*, 2301312.
[30] H.-B. Sun, S. Kawata, *J. Light. Technol.* **2003**, *21*, 624.
[31] G. Zyla, G. Maconi, A. Nolvi, J. Marx, D. Ladika, A. Salmi, V. Melissinaki, I. Kassamakov, M. Farsari, *Light: Adv. Manuf.* **2024**, *5*, n/a.
[32] L. Siegle, S. Ristok, H. Giessen, *Opt. Express* **2023**, *31*, 4179.
[33] O. Tsilipakos, A. Xomalis, G. Kenanakis, M. Farsari, C. M. Soukoulis, E. N. Economou, M. Kafesaki, *Sci. Rep.* **2020**, *10*, 17653.
[34] A. Xomalis, O. Tsilipakos, M. Manousidaki, O. Busquets, G. Kenanakis, S. Tzortzakis, M. Farsari, C. Soukoulis, E. Economou, M. Kafesaki, *ACS Appl. Opt. Mater.* **2022**, *1*.
[35] J. K. Gansel, M. Thiel, M. S. Rill, M. Decker, K. Bade, V. Saile, G. von Freymann, S. Linden, M. Wegener, *Science* **2009**, *325*, 1513.
[36] G. Dolling, C. Enkrich, M. Wegener, C. M. Soukoulis, S. Linden, *Science* **2006**, *312*, 892.
[37] S. Papamakarios, O. Tsilipakos, I. Katsantonis, A. D. Koulouklidis, M. Manousidaki, G. Zyla, C. Daskalaki, S. Tzortzakis, M. Kafesaki, M. Farsari, *ACS Photonics* **2024**.
[38] K. Vanmol, A. A. A. Nazar, H. Thienpont, F. Ferranti, J. V. Erps, *Opt. Express, OE* **2024**, *32*, 10190.
[39] Z. Wang, Y. Wu, D. Qi, W. Yu, H. Zheng, *Opt. Laser Technol.* **2024**, *169*, 110128.
[40] A. Ottomaniello, P. Vezio, O. Tricinci, F. M. D. Hoed, P. Dean, A. Tredicucci, V. Mattoli, *Nanophotonics* **2023**, *12*, 1557.
[41] M. McLamb, S. Park, V. P. Stinson, Y. Li, N. Shuchi, G. D. Boreman, T. Hofmann, *Optics* **2022**, *3*, 70.
[42] P. Somers, A. Münchinger, S. Maruo, C. Moser, X. Xu, M. Wegener, *Nat. Rev. Phys.* **2023**, 1.
[43] P. Somers, Z. Liang, J. E. Johnson, B. W. Boudouris, L. Pan, X. Xu, *Light Sci. Appl.* **2021**, *10*, 199.
[44] W. Ouyang, X. Xu, W. Lu, N. Zhao, F. Han, S.-C. Chen, *Nat. Commun.* **2023**, *14*, 1716.
[45] P. Kiefer, V. Hahn, S. Kalt, Q. Sun, Y. M. Eggeler, M. Wegener, *Light Adv. Manuf.* **2024**, *4*, 28.
[46] C. Cao, J. Liu, X. Xia, X. Shen, Y. Qiu, C. Kuang, X. Lui, *Addit. Manuf.* **2022**, *51*, 102658.
[47] C. Cao, X. Xia, X. Shen, X. Wang, T. Yang, Q. Liu, C. Ding, D. Zhu, C. Kuang, X. Lui, *Nat. Commun.* **2024**, *15*, 9216.
[48] C. Cao, G. Lingling, X. Shen, X. Xia, Y. Qiu, H. Wang, Z. Yang, D. Zhu, C. Ding, C. Kuang, X. Lui, *Addit. Manuf.* **2023**, *74*, 103740.
[49] X. Zhou, Y. Hou, J. Lin, *AIP Adv.* **2015**, *5*, 030701.
[50] I. Sakellari, E. Kabouraki, D. Gray, V. Purlys, C. Fotakis, A. Pikulin, N. Bityurin, M. Vamvakaki, M. Farsari, *ACS Nano* **2012**, *6*, 2302.
[51] G. Kenanakis, A. Xomalis, A. Selimis, M. Vamvakaki, M. Farsari, M. Kafesaki, C. M. Soukoulis, E. N. Economou, *ACS Photonics* **2015**, *2*, 287.
[52] S. Juodkazis, V. Mizeikis, K. K. Seet, M. Miwa, H. Misawa, *Nanotechnol.* **2005**, *16*, 846.
[53] E. Skliutas, D. Samsonas, A. Čiburys, L. Kontenis, D. Gailevičius, J. Berzinš, D. Narbutis, V. Jukna, M. Vengris, S. Juodkazis, M. Malinauskas, *Virtual Phys. Prototyp.* **2023**, *18*, 2228324.
[54] M. Stavrou, G. Zyla, D. Ladika, F. Dumur, M. Farsari, D. Gray, *ACS Appl. Opt. Mater.* **2024**, *2*, 1653.
[55] N.-H. Shen, M. Massaouti, M. Gokkavas, J.-M. Manceau, E. Ozbay, M. Kafesaki, T. Koschny, S. Tzortzakis, C. M. Soukoulis, *Phys. Rev. Lett.* **2011**, *106*, 3.
[56] O. Tsilipakos, L. Zhang, M. Kafesaki, C. M. Soukoulis, T. Koschny, *ACS Photonics* **2021**, *8*, 1649.
[57] O. Tsilipakos, L. Maiolo, F. Maita, R. Beccherelli, M. Kafesaki, E. E. Kriezis, T. V. Yioultsis, D. C. Zografopoulos, *Appl. Phys. Lett.* **2021**, *119*, 23.
[58] M. Kafesaki, T. Koschny, R. S. Penciu, T. F. Gundogdu, E. N. Economou, C. M. Soukoulis, *J. Opt. A: Pure Appl. Opt.* **2005**, *7*, S12.
[59] J.-N. Liu, M. V. Schulmerich, R. Bhargava, B. T. Cunningham, *Opt. Express* **2011**, *19*, 24182.
[60] G. Quaranta, G. Basset, O. J. F. Martin, B. Gallinet, *Laser Photonics Rev.* **2018**, *12*, 1800017.
[61] A. Ferraro, D. C. Zografopoulos, R. Caputo, R. Beccherelli, *Appl. Phys. Lett.* **2017**, *110*, 141107.
[62] Okmetic Oy, SOI wafers - Silicon-On-Insulator line, **2024**, https://www.okmetic.com/silicon-wafers/soi-wafers-silicon-on-insulator-line/ (accessed: January 2024).

[63] J.-P. Hugonin, P. Lalanne, Light-in-complex-nanostructures/RETICOLO:V9, **2021**, https://zenodo.org/record/5905381 (accessed: January 2024).
[64] P. Lalanne, G. M. Morris, *J. Opt. Soc. Am. A, JOSAA* **1996**, *13*, 779.
[65] D. Chandler-Horowitz, P. M. Amirtharaj, *J. Appl. Phys.* **2005**, *97*, 123526.
[66] J. Kischkat, S. Peters, B. Gruska, M. Semtsiv, M. Chashnikova, M. Klinkmüller, O. Fedosenko, S. Machulik, A. Aleksandrova, G. Monastyrskyi, Y. Flores, W. Ted Masselink, *Appl. Opt.* **2012**, *51*, 6789.
[67] A. Žukauskas, I. Matulaitienė, D. Paipulas, G. Niaura, M. Malinauskas, R. Gadonas, *Laser Photonics Rev.* **2015**, *9*, 706.
[68] A. Žukauskas, G. Batavičiūtė, M. Ščiuka, Z. Balevičius, A. Melninkaitis, M. Malinauskas, *Opt. Mater.* **2015**, *39*, 224.
[69] G. Balčas, M. Malinauskas, M. Farsari, S. Juodkazis, *Adv. Funct. Mater.* **2023**, *33*, 2215230.
[70] A. Vyatskikh, R. C. Ng, B. Edwards, R. M. Briggs, J. R. Greer, *Nano Lett.* **2020**, *20*, 3513.
[71] S.-F. Liu, Z.-W. Hou, L. Lin, Z. Li, H.-B. Sun, *Adv. Funct. Mater.* **2023**, *33*, 2211280.
[72] F. M. den Hoed, A. Ottomaniello, O. Tricinci, L. Ceseracciu, M. Carlotti, P. Raffa, V. Mattoli, *Adv. Funct. Mater.* **2023**, *33*, 2214409.
[73] Z. Ma, T. Li, X. Dai, X. Shen, X. Wang, H. Fu, X. Xia, Q. Zhu, Q. Zhu, Z. Yu, C. Cao, S. You, C. Kuang, *Adv. Funct. Mater.* **2024**, *34*, 2409859.
[74] C. Maibohm, O. F. Silvestre, J. Borme, M. Sinou, K. Heggarty, J. B. Nieder, *Sci. Rep.* **2020**, *10*, 8740.
[75] B. Jiao, F. Chen, Y. Liu, X. Fan, S. Zeng, Q. Dong, L. Deng, H. Gao, W. Xiong, *Int. J. Extrem. Manuf.* **2023**, *5*, 035008.
[76] S. K. Saha, D. Wang, V. H. Nguyen, Y. Chang, J. S. Oakdale, S.-C. Chen, *Science* **2019**, *366*, 105.
[77] G. Seniutinas, A. Weber, C. Padeste, I. Sakellari, M. Farsari, C. David, *Microelectron. Eng.* **2018**, *191*, 25.
[78] D. Ladika, A. Butkus, V. Melissinaki, E. Skliutas, E. Kabouraki, S. Juodkazis, M. Farsari, M. Malinauskas, *Light Adv. Manuf.* **2024**, *5*, 48.
[79] P. Somers, Z. Liang, T. Chi, J. E. Johnson, L. Pan, B. W. Boudouris, X. Xu, *Nanophotonics* **2023**, *12*, 1571.
[80] J. Fischer, M. Wegener, *Laser Photonics Rev.* **2013**, *7*, 22.
[81] Z. Gan, Y. Cao, R. A. Evans, M. Gu, *Nat. Commun.* **2013**, *4*, 2061.
[82] G. Merkininkaitė, E. Aleksandravičius, S. Varapnickas, D. Gailevičius, S. Šakirzanovas, M. Malinauskas, in R. Stoian, J. Bonse, editors, *Ultrafast Laser Nanostructuring: The Pursuit of Extreme Scales*, Springer Series in Optical Sciences, 787–823. Springer Cham, **2023**.
[83] W. Wang, Y. Liu, Z. Xie, *J. Bionic Eng.* **2021**, *18*, 1011.
[84] T. Li, L. Li, L. Jiang, P. Yi, M. Li, S. Li, X. Li, X. Zhang, A. Wang, Z. Wang, J. Li, L. Huang, B. Han, X. Li, *Adv. Opt. Mater.* **2024**, *12*, 2400612.